ACS Sustainable Chemistry & Engineering

Research Article

pubs.acs.org/journal/ascecg

Development of Sustainable Rapid Microwave Assisted Process for Extracting Nanoporous Si from Earth Abundant Agricultural Residues and Their Carbon-based Nanohybrids for Lithium Energy Storage

S. Praneetha and A. Vadivel Murugan*

Advanced Functional Nanostructured Materials Laboratory, Centre for Nanoscience and Technology, Madanjeet School of Green Energy Technologies, Pondicherry University (A Central University), Pondicherry 605014, India

Supporting Information

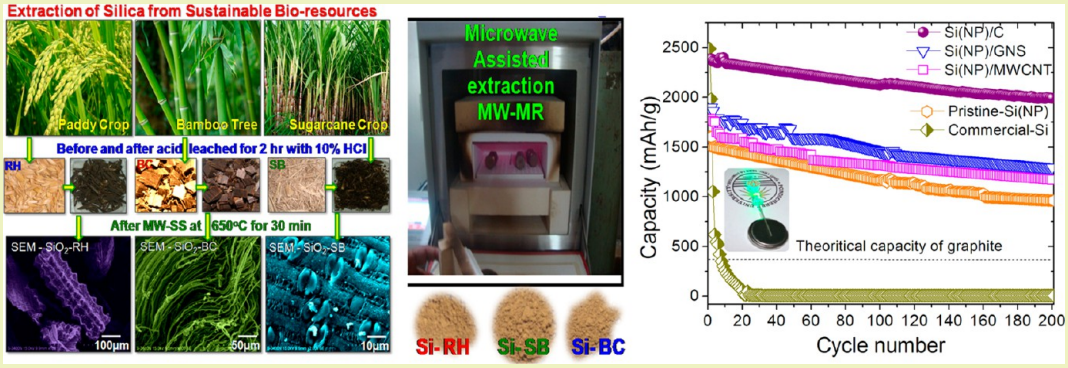

ABSTRACT: Bamboo culm (BC), rice husk (RH), and sugarcane bagasse (SB) are the most earth abundant, low-cost, and eco-friendly agricultural residues that contain a substantial amount of biogenic silica (SiO_2) in the form of amorphous hydrated silica grains. In this study, we successfully extracted SiO_2 from various agricultural residues such as BC, RH, and SB via rapid microwave assisted solid-state ashing (MW-SS), followed by microwave assisted magnesiothermic reduction (MW-MR) of SiO_2 into crystalline silicon (Si) at <650 °C for 30 min without the need for a reducing gas atmosphere. The MW-MR process further supports the development of an interconnected three-dimensional porous Si network with a pore diameter of 50−80 nm and wall thickness of ∼23 nm. The obtained Si is further decorated with dimensionally modulated carbon-based materials such as carbon (C), graphene nanosheets (GNS), and multiwall carbon nanotubes (MWCNT), which can offer higher delithiation capacities (1997, 1290, and 1166 mAh g^{-1}, respectively) compared to pristine Si (956 mAh g^{-1}) extracted from RH at C/5 rate after 200 cycles. These results suggest that the earth-abundant BC, RH, and SB could be sustainable resources for large-scale production of nanoporous crystalline Si, which has been extracted via an energy efficient, low-cost microwave assisted sustainable process for lithium ion battery anodes.

KEYWORDS: *Sugarcane bagasse, bamboo culm, rice husk, biogenic-silicon nanoporous, graphene, multiwall carbon nanotubes, anode material, microwave, lithium energy storage*

INTRODUCTION

Global energy consumption is anticipated to be nearly 7.8 × 10^{20} J in 2035. The fluctuation in natural-gas and oil prices has impelled every person to seriously look into the issues dealing with our energy supply and demand. To meet the increasing energy demands in the near future, it is our necessity to search for the development of sustainable functional materials via low-cost chemical synthesis processes for clean energy conversion and storage technologies.[1−5] Recently, nanoscale Si has been of enormous interest for various potential applications.[3−12] However, the worldwide conventional blast-furnace production of synthetic metallurgical-grade (MG) Si yields >95% purity and involves much higher production temperatures of >1900 °C, which is insufficient for our current needs in electronic and solar cells industries. The energy input for this process is ∼50 kWh/kg and the current worldwide production of MG-Si is ∼1 million tons/year, which releases several million tons of greenhouse gas CO_2 into the atmosphere.[9,10] Therefore, worldwide efforts are being directed to develop a low-cost, high-volume, and commercially sustainable process for production of high purity Si for clean energy technological applications. Conspicuously, the amount of metallurgical-grade (MG) silicon manufactured via blast-furnace is minuscule compared to the amount of silicon (orthosilicic acid-silica-

Received: August 11, 2014
Revised: December 22, 2014
Published: January 12, 2015

DOI: 10.1021/sc500735a
ACS Sustainable Chem. Eng. 2015, 3, 224−236

orthosilicic acid) cycled through vegetation. It is estimated that, globally, plants uptake 1.7−5.6 billion tons of silicon/year,[11,12] particularly the earth-abundant and most important Poaceae-family of *Saccharum officinale* (sugarcane), *Bambusoideae bambuseae* (bamboo), and *Oryza sativa* (rice), which are well established as "silicon accumulators".[11−14] For such plants, the beneficial effect of SiO_2 on growth plays a significant function in defending themselves from exterior invasion by parasites, insects, herbivores, and simultaneously make possible ventilation between the interior and exterior of plants to conserve moisture and nutrients inside the kernel.[3,13−16] To accomplish these essential twin-functions, the SiO_2 in the plants has developed distinctive porous-structures throughout the natural evolution.

Recently, nanostructured Si has been considered as the next-generation anode material for the lithium battery that has attracted incredible interest due to its enormously high theoretical capacity of about ∼4200 mAh g^{-1} ($Li_{4.4}Si$), which is comparatively higher than the theoretical capacity of currently used graphite (372 mAh g^{-1} for compound LiC_6) and Li alloys.[17−23] Nevertheless, Si-based anodes also undergo significant challenges and it has been demonstrated that they have shown large volume expansion (ca. 400%), solid electrolyte interphase (SEI) layer formation on the Si surface, and subsequently undergo rapid capacity fading during lithiation and delithiation processes. Such a dramatic change in volume can induce large strain, followed by the pulverization of Si after a few cycles that hampers their use in practical applications as the anode in rechargeable lithium ion batteries for electric and hybrid vehicles.

As of now, extensive studies have been made to surmount these challenges via tuning of Si morphology into nanospheres, nanoporous, nanowire, and core−shell carbon coated on Si nanofibers via various methodologies that exhibit longer cycling life when compared to micrometer size Si.[24−26] Moreover, agricultural residues such as bamboo culm (BC), rice husk (RH), and sugarcane bagasse (SB) are attractive raw materials, where silicon (Si) occurs in nature as SiO_2 microassemblies.[11,12] Interestingly, extraction of value-added functional materials from agricultural residues via sustainable clean and energy-efficient processes have drawn much attention in recent years. Although microwave assisted hydro/solvothermal (MW-HT/ST) methods have been used for synthesis of various nanostructured materials,[27−29] to our knowledge, extraction of value-added materials from various agricultural residues via microwave assisted methods has yet to be studied. Sustainable MW assisted synthesis processes are gaining wide attraction, as they provide a clean, rapid, low-cost, and energy-efficient method.

We demonstrate here a rapid microwave assisted approach to extract SiO_2 from various agricultural residues such as BC, RH, and SB followed by metallothermic reduction of SiO_2 into elemental silicon (Si) within 30 min at temperatures <650 °C without requiring any reducing gas atmosphere. This "metallurgy in a Swagelok" reactor inside the microwave muffle furnace can be provided by the SiC passive heating element (PHE) plates by absorbing microwave radiation and subsequent transfer of heat to the reactants with increase in reaction kinetics during the raw material (SB, BC, and RH) ashing and metallothermic reduction processes. To produce Si-based nanohybrids, we adopted a MW-ST process that offered a uniform heating of polar solvent by absorbing microwave energy followed by heating. The application potential of the obtained pristine Si from RH and their nanohybrids with carbon, multiwall carbon nanotubes, and graphene is also demonstrated as a high capacity anode for lithium ion batteries for energy storage applications.

MATERIALS AND METHODS

Extraction of SiO_2 from SB, BC, and RH via MW-SS Method. The naturally occurring agricultural residue such as SB was obtained from a sugarcane industry, BC from our university garden, and RH from rice mills in-and-around Pondicherry, India. They were further cleaned with water to eliminate soils, dirt, and subsequently dried in sunlight. Twenty-four grams of dried raw material (SB, BC, and RH) was refluxed with 400 mL of 90:10 v/v of H_2O and HCl (35%) for 2 h. The acid-leached raw material was cleaned with distilled water until the pH value was ∼5. Then it was dried in an oven at 80 °C followed by the MW-SS heating process, illustrated in Figure 1, employing a Milestone PYRO microwave muffle furnace ashing system by using a quartz fiber crucible (QFC) (advantages of QFC: after ashing at 650 °C, we can take out immediately from furnace and it cools within a few seconds time). The PYRO system dramatically reduced the ashing time, often from many hours to a few minutes, and subsequently reduced energy consumption, cost, and also offered the most facile way to ash the samples with safety. The microwave exposure time of ∼20 min ramping and holding 10 min at a temperature of 650 °C was programmed with the Milestone software. Continuous monitoring and control of the internal temperature (±1 °C) was facilitated by the automatic temperature controls system. Reaction parameters (time and temperature) were automatically adjusting using applied power (0−1000 W). The microwave-furnace was functioned with full power of 1200 W at a frequency of 2.45 GHz. High surface area of white biogenic SiO_2 powder was obtained from different agricultural residues, as illustrated in Figure 1. The chemical compositions and SiO_2 obtained from RH, BC, and SB after burning out into ash (before acid treatment) was further analyzed by using X-ray fluorescence (WD-XRF Bruker, S4 Pioneer), as shown in the Supporting Information (Table S1).

Microwave Assisted Metallothermic Reduction (MW-MR) of SiO_2 into Nanoporous Si. The obtained biogenic SiO_2 (3.6 g) from the MW-SS method was completely mixed with 2.9 g of magnesium (Mg) metal powder (Merck 99%). The mixed powder was filled in a "Swagelok reactor". The sealed reactor was kept inside the microwave muffle furnace, and the reduction process is illustrated in Figure 1. The microwave exposure time of ∼20 min ramping and 10 min holding at a temperature of 650 °C for magnesium were programmed with the software automatically adjusting the applied power (0−1000 W) with an operated frequency of 2.45 GHz. After the MW-SS process, the "Swagelok reactor" was removed from the microwave muffle furnace. The obtained brownish-black colored powder consisted of Si, Mg_2Si, and MgO, which was slowly added into a solution mixture of HCl, H_2O, and ethanol (19.3:28.3:172.6 mL) followed by stirring for 6 h to remove Mg_2Si and MgO from Si. The solution mixture was centrifuged and subsequently washed with an excess of distilled water until the pH dropped down to neutral. The Si-containing solution was centrifuged and washed with water and ethanol (no differences were noticed without HF etching). Finally, 1.15 g of dark yellowish colored fine Si nanopowder was obtained after the solution was dried in a vacuum oven at 40 °C for 6 h. Recently, Choi et al. and Cui et al. reported SiO_2 to Si conversion yields of ∼64% and 89%, respectively. The detailed experimental conditions and yield are provided in Table S2 in the Supporting Information. Experimentally, we obtained SiO_2 to Si conversion yield of ∼68% by this MW-MR method, which was heated at 650 °C for 1/2 h. To find out the SiO_2-to-Si conversion yield with respect to temperature variation (fixed SiO_2 to Mg weight ratio), we have also demonstrated SiO_2 to Si reduction by a conventional tubular furnace that was heated at 600 to 900 °C for 3 h in an Ar atmosphere. However, the MW-MR method was carried out at 600 to 900 °C for 1/2 h without the need for a reducing gas atmosphere. A comparative bar chart is shown in the Supporting Information, Figure S5.

DOI: 10.1021/sc500735a
ACS Sustainable Chem. Eng. 2015, 3, 224−236

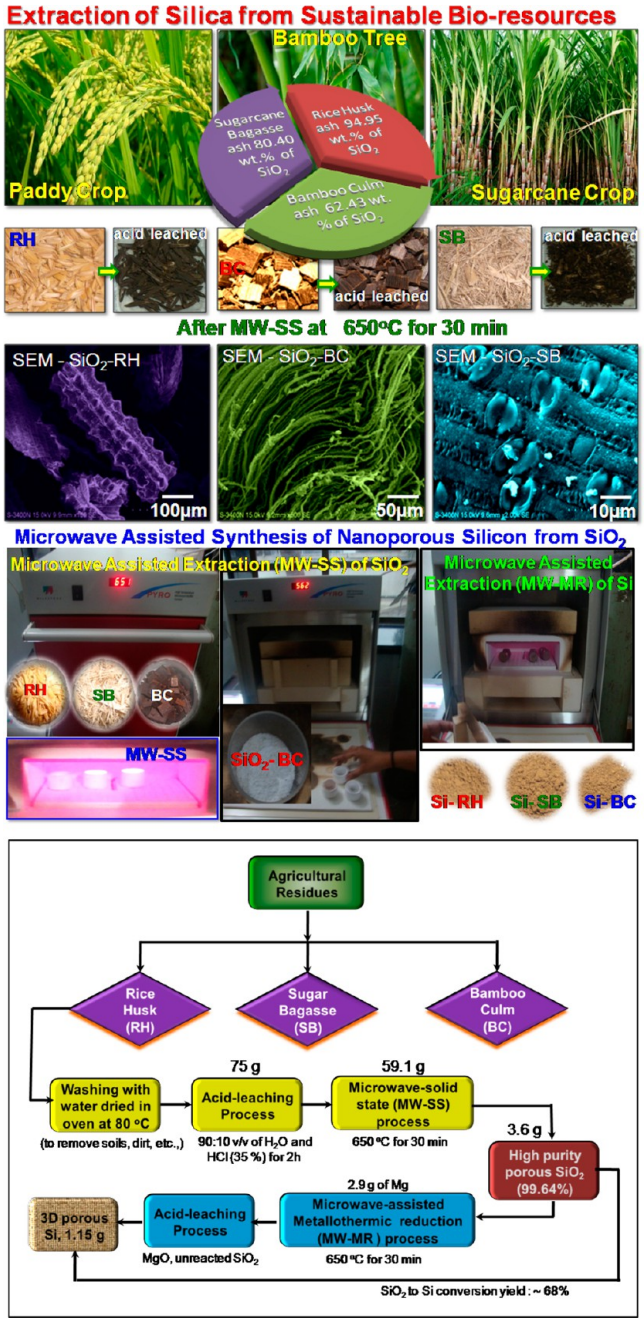

Figure 1. Schematic illustration of biogenic SiO_2 powder extracted from different bioresources such as sugar bagasse (SB), bamboo culm (BC), and rice husk (RH) via microwave assisted solid state (MW-SS) ashing and 3D nanoporous silicon (Si) synthesized by magnesiothermic reduction of biogenic silica via the microwave assisted (MW-MR) process for 30 min at 650 °C without the need for a reducing gas atmosphere. Digital photographic images of before and after acid-leached SB, BC, and RH raw materials are also shown. SEM images of the SB-, BC-, and RH-originated silica seen from the outer surface. Flowchart summarizing the synthetic procedures to obtain 3D nanoporous Si from rice husk with SiO_2 to Si conversion yield.

Preparation of Si-based Nanohybrids. *Ex Situ Carbon Coating on Nanoporous Si (MW-SS).* The obtained Si nanoporous powders (from MW-SS method) were mixed with sucrose powder and subsequently carbonized inside the "Swagelok reactor" in the Ar-filled glovebag (Aldrich). The sealed reactor was kept inside the microwave muffle furnace, and the carbonization process is illustrated in Figure 2. The microwave exposure time of ~20 min ramping and 10 min holding at a temperature of 600 °C was maintained. After the MW-SS method, the "Swagelok reactor" was removed from the microwave muffle furnace. Finally, a black colored powder of carbon coated Si was obtained with the final weight ratio of Si:C optimized to 90:10 wt %.

Ex Situ MWCNT Nanonetworking with Si Nanocrystals (MW-ST). Complete details of the preparation method for synthesis of acid-functionalized MWCNT (diameter ~20−30 nm) were adopted as per our previous report.[25] Ten weight percent MWCNT in ethylene glycol was then mixed with the Si nanocrystals powder by magnetic stirring for 20 min to ensure complete mixing. The Si-MWCNT hybrid was centrifuged and subsequently washed with excess of acetone and then dried in a vacuum oven at 80 °C for 30 min. The weight percent of Si to MWCNT in the mixture was 90:10. The preparation process is illustrated in Figure 2.

In Situ Decoration of Si Nanocrystals on Graphene Nanosheets (GNS) by MW-ST Method. The Graphene oxide (GO) was prepared according to the modified Hummer's method as per our previous report.[29] Further, the obtained GO was subjected to lyophilization by mechanical refrigeration by drying GO solution into nanostructured GO foam as shown in the Supporting Information, Figure S1. Si nanocrystals obtained from the MW-SS process and GO nanofoam were dissolved in ethylene glycol (EG) in a quartz vessel and stirred to get a slurry (it was optimized and the Si to GNS weight ratio was 90:10 after MW-ST synthesis). The slurry containing Si nanocrystals and GO was transferred to a quartz vessel fitted with a probe (to measure temperature and pressure inside the vessel), housed in a sturdy thermowell and protected from chemical environment. The rotor containing the sealed quartz vessels was then placed on a turnable for uniform heating in an Anton-Paar microwave synthesis system (Figure 2). Decoration of Si nanocrystals on GNS was carried out simultaneously during this solvothermal process inside the quartz vessels at a temperature of 180 °C in EG for 10 min, and the vessels were then cooled to room temperature by an inbuilt cooling fan. The supernatant EG solvent was carefully decanted, and the resulting black color Si/GNS hybrid was washed repeatedly by ethanol until the washings were colorless to ensure complete removal of EG, as shown in Figure 2.

Characterizations. X-ray diffraction (XRD) analysis of the samples was performed by a Rigaku Ultima IV X-ray diffractometer using filtered Cu Kα radiation to examine the crystal structures of SiO_2 and Si extracted from the BC/SB/RH. Their morphologies were characterized by field emission scanning electron microscopy (FE-SEM) Caral Zeiss SUPRA-55 and HR-TEM (FEI; Tecnai G2F30) equipment, respectively. SEM-EDS was used for elemental analysis. Raman spectroscopic studies were carried out with a Renishaw inVia system using excitation energy of a 514 nm laser. X-ray photoelectron spectroscopy (XPS) was carried out in a VG Microtech Multilab ESCA 3000 spectrometer using a nonmonochromatized Al Kα X-ray source ($h\nu$ = 1486.6 eV). The base pressure in the analysis chamber was maintained in the 10^{-10} Torr range. The energy resolution of the spectrometer was set up at 1.1 eV with Al Kα radiation at a pass energy of 50 eV. Binding energy (BE) calibration was demonstrated with Au $4f_{7/2}$ core level at 83.9 eV. All the BE values thus reported here have error values ranging within ±0.1 eV. Thermogravimetric analysis (TGA-DTA) was performed with a TA Instruments (Q600SDT) thermal analysis system using dry oxygen as a carrier gas. The TGA experiments were performed from room temperature to 1000 °C at a heating rate of 10 °C min^{-1}. The carbon content (weight percent) in the Si/C hybrid was obtained from the TGA analysis.

Electrochemical performances were evaluated with a CR2032 coin cell with an Arbin battery cycler (BT2000). The coin cells were fabricated with Si nanocrystals obtained from the RH- and Si-based nanohybrid (Si/C; Si/GNS; Si/MWCNT) anode; metallic foil lithium was used as both the reference and counter electrodes. Si powder, carbon black (super-P), and polyvinylidene fluoride (PVDF) binder were blended with NMP (1-methyl-2-pyrrolidinone) by magnetic stirring until a homogeneous slurry was prepared, and then the slurry was casted on copper foil and fabricated as a thin film electrode. The electrode was dried at room temperature as well as 115 °C for 12 h under vacuum. The electrolyte solution consisted of 1.0 M $LiPF_6$ in

DOI: 10.1021/sc500735a
ACS Sustainable Chem. Eng. 2015, 3, 224−236

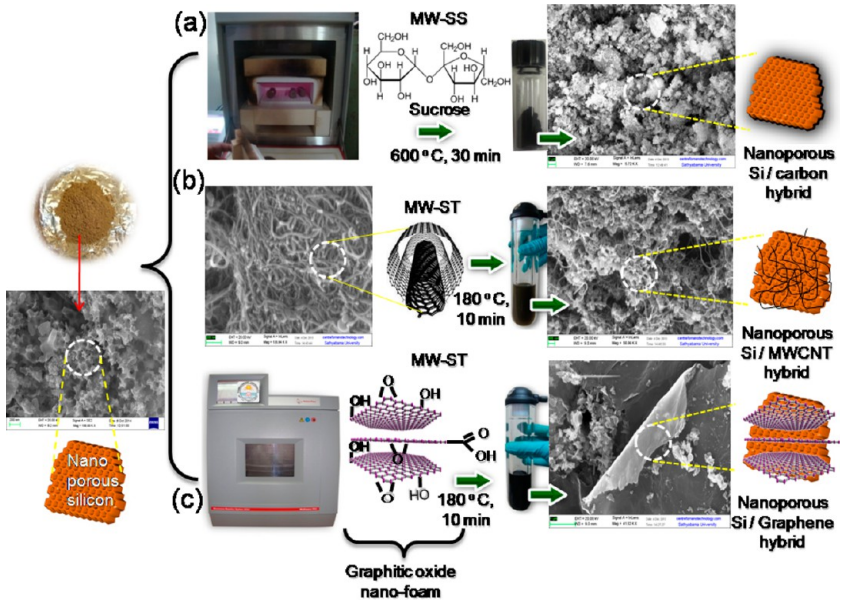

Figure 2. Schematic representation of silicon-based nanohybrid prepared by (a) microwave assisted solid state (MW-SS) decoration of carbon on 3D nanoporous silicon at 600 °C within 30 min, (b) microwave assisted solvothermal (MW-ST) synthesis of silicon and MWCNT nanonetworking at 180 °C in 10 min, and (c) in situ one-pot MW-ST synthesis of 3D nanoporous silicon decorated on graphene nanosheets (GNS) at 180 °C in 10 min.

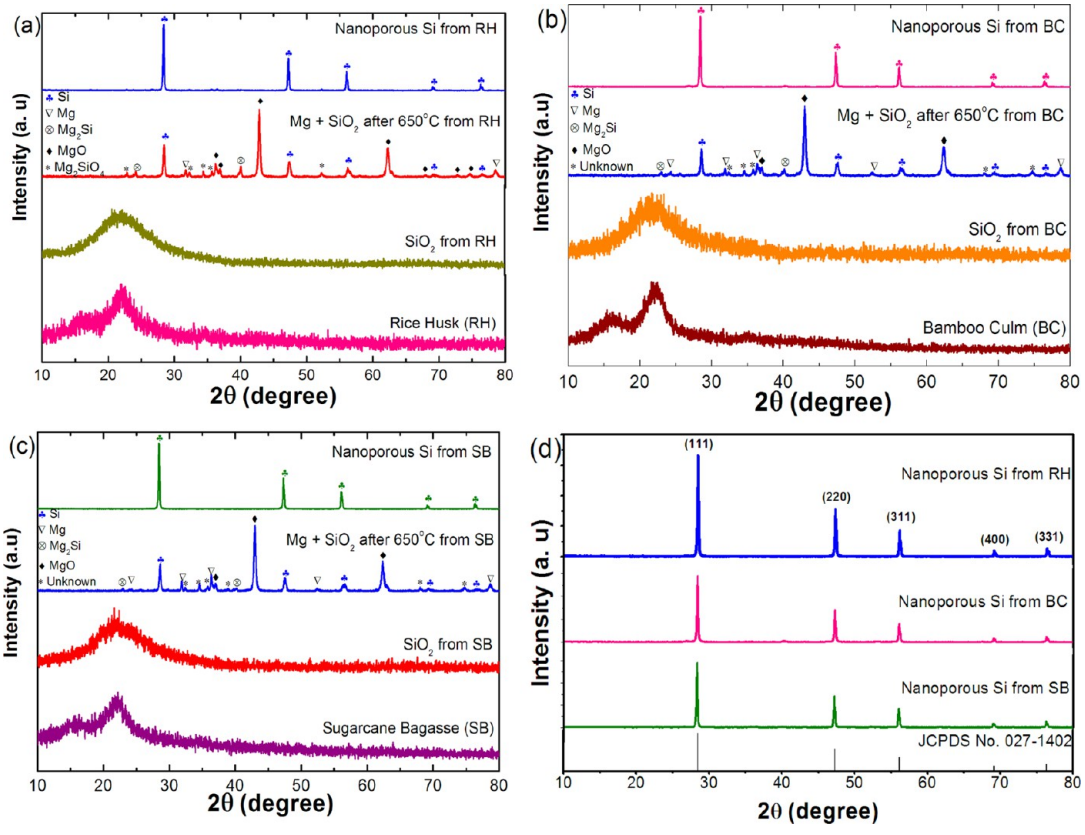

Figure 3. X-ray diffraction patterns of biogenic SiO_2 and nanoporous Si synthesized from different natural resources like (a) RH, (b) BC, and (c) SB via MW-SS and MW-MR methods at 650 °C in 30 min. For comparative study, XRD patterns of the raw materials of SB, BC, and RH contain amorphous SiO_2, XRD patterns of the mixture, revealing the formation of Si, MgO, and Mg_2Si after magnesiothermic reduction (MW-MR) (before HCl washings) are also provided, and (d) XRD patterns of the 3D nanoporous silicon obtained from RH, BC, and SB via the MW-MR method with a temperature of 650 °C in 30 min.

ethylene and dimethyl carbonate (EC/DMC, 1:1 v/v) with 2 wt % vinylene carbonate (VC). To improve the cycling performance, we added VC additive into the electrolyte, and a Celgard 2250 polypropylene was used as a separator. The coin cells were cycled at different rates between 0.01 and 1.0 V versus Li/Li^+. The electrode was prepared by mixing 80 wt % active materials with 10 wt % super-P

DOI: 10.1021/sc500735a
ACS Sustainable Chem. Eng. 2015, 3, 224−236

carbon and 10 wt % PVDF binder, and the active material loading amount was 20 mg cm^{-2}. The super-P, which acted only as a conducting agent, did not contribute to the total capacity. The coin cells were assembled in an argon-filled MBraun-Unilab glovebox, GmbH. The specific capacity was calculated based on the Si mass. The lithiation/delithiation rate was calculated by assuming the theoretical capacity of Si (4200 mAh g^{-1}). The Coulombic efficiency was calculated as *C*-delithiated/*C*-lithiated (*C* is the capacity of the anode during lithiation/delithiation process). For comparison purposes, commercially available Si (nanocrystalline, particle size ranging from 100 to 200 nm, 98% Sigma-Aldrich) was fabricated in the same manner and evaluated with Si nanocrystals extracted from RH. The structural change of the Si electrode was investigated after 100 cycles. The cell was disassembled in an Ar-filled glovebox. An excess of acetonitrile was used to remove remaining electrolyte ($LiPF_6$ salt) on the electrode. Subsequently, the electrodes were further soaked in 0.5 M HCl and washed with doubly distilled water and then dried in a vacuum oven for 30 min to remove SEI layer formation on the electrodes. The morphology of the electrode was observed by FE-SEM. Electrochemical impedance (EIS) studies were performed at 1.5 V with an amplitude of 5 mV in the frequency between 100 kHz and 10 mHz.

RESULTS AND DISCUSSION

Synthesis of Si from SiO_2 (SB, BC, and RH) by MW-SS Method and XRD Characterization. The mechanism of the MW-SS process involves the following: first, microwave irradiation was absorbed by the SiC passive heating element (PHE) plates followed by a hot zone that developed rapidly inside the furnace. Subsequently, the heat is transferred to the raw material (SB, BC, and RH) uniformly, which reduces thermal gradients inside the "Swagelok reactor" and enhances the reaction kinetics. In the first step of the MW-SS method, SB, BC, and RH raw materials were pyrolyzed at 650 °C via the MW-SS method and subsequently we obtained a white porous SiO_2 powder within 30 min. Figure 3a−c shows the XRD pattern of the raw material of SB, BC, and RH as such received from agricultural residues. Figure 3a−c shows XRD profiles of biogenic SiO_2 obtained from different agricultural residues that endure the MW-SS ashing method at 650 °C in 30 min. The three XRD patterns are very close to each other and illustrate that the silica samples are amorphous in nature. This also suggests that the MW-SS is an effective process to extract high content of SiO_2, which is consistent with the X-ray fluorescence (XRF) results. Figure 3a−c shows XRD patterns of magnesiothermic reduction of Mg/SiO_2 at 650 °C via the MW-SS method. During the rapid MW-MR, Si has been formed via the solid-state redox reaction between Si and Mg. XRD analysis further confirmed the presence of elemental crystalline Si along with MgO, Mg_2Si, and Mg_2SiO_4 impurities in the reacted sample, and the reactions can be summarized as follows

$$SiO_2(s) + 2Mg(g) \rightarrow Si(s) + 2MgO(s) \quad \Delta H = -546.42\ kJ\ mol^{-1} \tag{1}$$

or

$$SiO_2(s) + 2Mg(s) \rightarrow Si(s) + 2MgO(s) \quad \Delta H = -291.62\ kJ\ mol^{-1} \tag{2}$$

If the amount Mg is more

$$2Mg(g) + Si(s) \rightarrow Mg_2Si(s) \quad \Delta H = -318.91\ kJ\ mol^{-1} \tag{3}$$

When the temperature is 650 °C in 30 min under MW-MR conditions and the Mg/SiO_2 ratio is 1:1, the XRD pattern clearly shows the presence of Si, MgO, and Mg_2Si peaks in Figure 3a−c. When the $MgO/Si/Mg_2Si$ composite mixtures were immersed in ethanol, HCl, and H_2O mixture, followed by an additional treatment in HF solution (No differences were noticed without HF etching), the obtained powder reflections corresponding to Si could be seen in the XRD (Figure 3a−c), which can be indexed into the pure phase of well-crystalline Si with a cubic structure (JCPDS No. 27-1402). The sharp diffraction peaks of Si demonstrates the highly crystalline nature that can be feasible by the MW-SS method within a short reaction time of 30 min at 650 °C. Figure 3d shows a consolidated XRD pattern of Si obtained from various agricultural residues such as SB, BC, and RH, indicating all of them are crystalline in nature. The energy dispersive X-ray (EDX) analysis also indicated that this acid treatment resulted in the selective and complete dissolution of MgO and Mg_2Si.

N_2 adsorption analysis can provide qualitative information on the adsorption process and the surface area available to the adsorbate. It is also a promising technique to measure the porous structures in materials. The porosity of the samples was investigated by nitrogen adsorption and desorption measurements (Brunauer−Emmett−Teller, BET), which suggests that the specific surface areas of the biogenic SiO_2 extracted from SB, BC, and RH were 238, 247, and 252 $m^2\ g^{-1}$, respectively. The surface areas of 3D porous elemental Si decreased considerably to 156, 168, and 172 $m^2\ g^{-1}$ obtained from SB, BC, and RH, respectively, which were much higher than that of the commercial Si (20 $m^2\ g^{-1}$). BJH (Barrett−Joyner−Halenda) analysis[30] of the N_2 desorption curves specified that the Si possessed a significant population of nanopores with a diameter of pore size ∼56 nm rather than the starting MgO/Si composite, which is in agreement with the above high resolution transmission electron microscopy (HR-TEM) observations. In addition, there is no diffraction peaks in the small-angle XRD, which implies pore structures in porous Si might be disordered.[31] Thermogravimetric analysis (TGA) curves of SB, BC, and RH raw materials heated in oxygen atmosphere are shown in the Supporting Information, Figure S2. They denoted that three steps of weight-loss occurred at the heating rate of 10 °C min^{-1}. The initial weight loss step (8, 10, and 11%), occurring at temperatures less than 100 °C for SB, BC, and RH, respectively, is due to water evaporation and the other residual solvent. The second major weight lose step (66, 68, 69%) corresponding to SB, BC, and RH at temperatures less than 400 °C is associated with the removal of volatile organic matter from the cellulosic structure. Volatilization for biomass samples of SB, BC, and RH initiated at approximately 210 °C, corresponding anticipated temperatures of 216, 227, and 229 °C, could be attributed to the pyrolysis of the major organic polymeric components such as α-cellulose, hemicellulose, and lignin. Finally, the basic structure is SiO_2 has been formed in the third step at temperatures >550 °C with a small amount of weight loss. Figure S3 in the Supporting Information shows the TGA-DTA plot of Mg powder and RH ash (SiO_2) mixture heated in N_2 atmosphere to determine the minimum temperature at which the reduction reaction (MW-MR) is activated. The DTA results show that multiple heat-release peaks have an onset temperature of 601.6 °C and the peak temperature of 613.6 °C, respectively. It is ascribed that the minimum temperature required for magnesiothermic reduction is ∼600 °C, thus the microwave assisted reduction temperature

DOI: 10.1021/sc500735a
ACS Sustainable Chem. Eng. 2015, 3, 224−236

was fixed at 650 °C. As temperature increases, the vapor pressure of magnesium inside the composite mix increases. Eventually, at microwave assisted temperatures ~580 °C, the vapor pressure is high enough, hence the reaction between Mg and SiO_2 can be activated. As the magnesiothermic reduction (exothermic) reaction proceeds, local temperatures are increased, resulting in more supply of Mg vapor at which the reduction reaction could be accelerated. However, the reaction rate was slowed down due to the formation of reduction products such as MgO and Si limits the diffusion of Mg into the SiO_2 core. This creates a concentration gradient for Mg from the surface to the reaction interface. Hence, at the outer layers, the conditions become thermodynamically favorable for the formation of Mg_2Si. Further reduction of SiO_2 is made possible through diffusion of Mg through the sandwiched product layer, consists of Mg_2Si, MgO and Si corroborated by the XRD patterns shown in Figure 3a−c.

FE-SEM and HR-TEM Analysis. Figure 4a−c illustrates SEM images of biogenic SiO_2 (SB, BC, and RH are burnt in air at 650 °C). The SEM micrograph (Figure 4c) of the RH biogenic silica ash shows the different types of prickly microhair cell that accumulates silica in the form of phytoliths. Silica that forms phytoliths in the BC protects the plant from various biotic and abiotic stresses. Figure 4a,b shows phytolith type in leaf sheaths that contain different types of bilobates in the SB and porous fiber like morphologies in BC. The phytoliths in sugarcane are amorphous silica ($SiO_2 \cdot nH_2O$) with trace amounts of crystalline quartz.[12] A well-organized corrugated outer epidermis and a thin lamellar inner epidermis was clearly visible after RH had been burned in air as shown in Figure 4c.

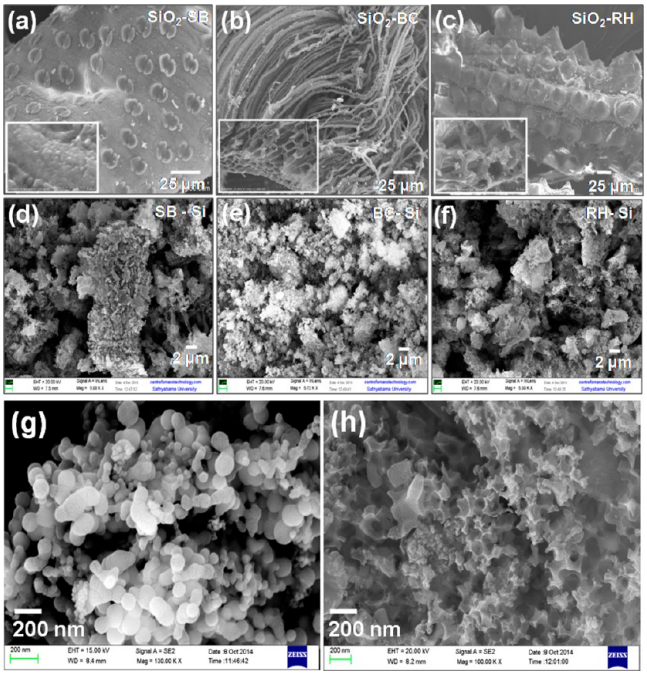

Figure 4. SEM micrographs of SiO_2 obtained from agricultural residues such as (a) SB, (b) BC, and (c) RH. FE-SEM micrographs (d−f) of nanoporous silicon synthesized via microwave assisted magnesiothermic reduction (MW-MR) of SiO_2 obtained from respective agricultural residues such as SB, BC, and RH. Comparative FE-SEM images of (g) commercially available agglomerated pristine Si and (h) nanoporous Si obtained from RH via microwave assisted magnesiothermic reduction (MW-MR) within 30 min at 650 °C.

The same morphology is observed and reported by Sharma et al.[32] Interestingly, SiO_2 is mostly located in both the outer and inner epidermis of RH as well as in the space between epidermis cells. When SB, BC, and RH are pyrolyzed, they showed many residual pores due to organic matters removed and become distributed within the ash sample. The result indicates that pyrolyzed SB, BC, and RH are porous materials which exhibit a large internal surface area. The SEM images of Si obtained from magnesiothermic reduction process of SiO_2 extracted from SB, BC, and RH, respectively, further confirms that the porous structures existing in the silicon material are interconnected (Figure 4d−f).

Further, the morphology and composition of the pristine Si_{RH}- and Si-based nanohybrids were characterized by FE-SEM and HR-TEM. Figure 4g illustrates the FE-SEM image of the polydispersed agglomerated commercial Si nanopowder, which was prepared by laser pyrolysis with particle sizes ranging from 100 to 200 nm without showing any porous structure morphology. In contrast, pristine Si_{RH} was prepared by the microwave assisted magnesiothermic reduction (MW-MR) (650 °C for 30 min) method and displayed a coherent interconnected 3D porous wall structure (Figure 4h) with relative uniformity. Thus, the FE-SEM image attributes that, during the MW-MR process, the Mg gas is able to infiltrate through the interconnected nanopores of the SiO_2 surface, and a homogeneously distributed Si/MgO mixture was formed. After removal of MgO by acid treatment of the Si/MgO mixture, the interconnected nanoporous wall structured Si was obtained in the MW-MR process.

The uniform pore-size distribution of the interconnected 3D-structured porous Si is also confirmed by high resolution transmission electron microscopy (HR-TEM; Figure 5a,b), which shows clearly that the pristine RH-orginated Si structure is composed of an interconnected nanoporous wall structure with a wall thickness of ~23 nm and a pore diameter of 50−80 nm. The EDX (Figure 5c) spectrum confirms the pure phase of the crystalline Si and also it substantiates the complete removal of the MgO and Mg_2Si via acid etching treatment. From ICP analysis, the purity of the Si_{RH} was 99.85%, thus XRD results corroborating that the pure Si phase was formed (Figure 3d). The HR-TEM image (Figure 5d) also exhibits Si(111) lattice fringes corresponding to a *d*-spacing value of 3.1 Å, demonstrating the crystalline nature of the Si. Further, the crystalline nature is also confirmed by selected-area electron diffraction (SAED), as shown in Figure 5e. This reveals a diffraction ring pattern corresponding to the diamond structured crystalline Si. Indeed, carbon coating was on the surface of the three-dimensional nanoporous Si, as shown in Figure 5f, and the coating thickness was measured to be ~4 nm, as shown in the HR-TEM image. Figure 5g illustrates the crystalline lattice fringes region related to the Si and carbon layer corresponding to the amorphous region. Such a nanohybrid architecture can provide an ultimate electron percolation pathway from the current collector to the whole surface area of the three-dimensional porous Si particle.[33,34]

FE-SEM micrographs of porous Si particle before and after decorating with carbon, graphene nanosheets (GNS), and MWCNT are shown in Figure S4a−f (Supporting Information). In this, as-synthesized pristine 3D porous Si particles obtained by the MW-MR method are shown in Figure S4a (Supporting Information), whereas Si decorated with carbon, MWCNT, and GNS are illustrated in Figure S4d−f (Supporting Information), respectively. Figure S4d,e (Support-

DOI: 10.1021/sc500735a
ACS Sustainable Chem. Eng. 2015, 3, 224−236

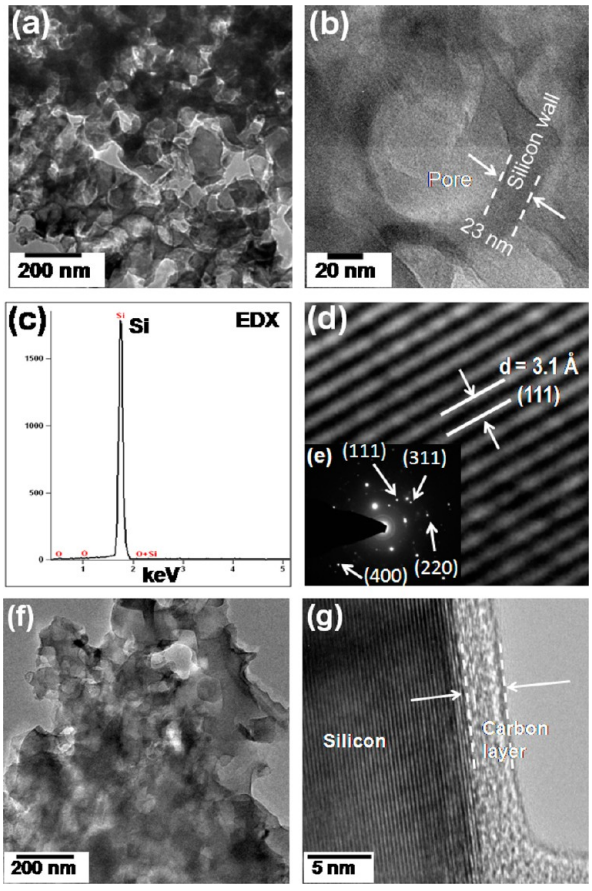

Figure 5. HR-TEM (a) overall image of the interconnected 3D porous structured Si, (b) image of the 3D porous Si wall structure. The wall thickness of Si is ~23 nm and the pore diameter is 50–80 nm. (c) EDX spectrum of the RH-derived Si and (d) HR-TEM image illustrating the (111) lattice fringes showing a *d*-spacing of 3.1 Å and (e) selected area electron diffraction (SAED) bright spots indexed, which correspond to the (111), (311), (220), and (400) lattices of Si [(e) lower inset)]. (f) HR-TEM images of Si/C nanohybrid revealing the preserved interconnected 3D-porous structure after the carbon coating and (g) HR-TEM images of Si/C enlightening 2–3 nm of carbon coating with dark crystalline fringes of Si.

ing Information) shows Si/C and Si/MWCNT were achieved by ex situ carbon coating on Si at 600 °C for 30 min via the MW-SS method and solution-based integration of MWCNT nanoscale networking with the Si nanohybrid. Figure S4f (Supporting Information) indicates an efficient in situ reduction of GO to GNS along with the 3D porous Si particle using ethylene glycol as a solvent via the MW-ST method at 180 °C within 10 min. Figure S4f (Supporting Information) shows Si nanocrystals decorated on the graphene sheets and that become homogeneously adhered to the surface of GNS. It is clearly shown that MWCNT and GNS become interconnected to the nanocrystals in close range, offering an extremely conductive pathway for the mobility of electrons during lithiation/delithiation process, and these nanohybrids also help buffer the volume change and reduce the irreversible capacities.

Raman Spectroscopy Characterization. Raman spectroscopy is considered to be a reliable tool to study the presence of both Si and carbon-based materials in the nanohybrids. Figure 6a shows the Raman spectra of the pristine silicon nanoparticles obtained from SB, BC, and RH,

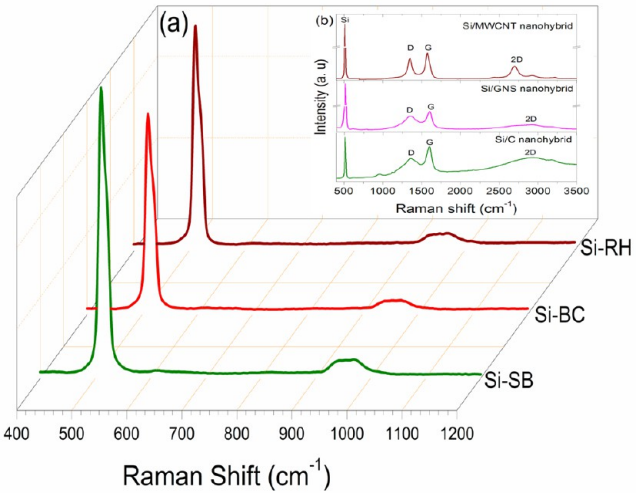

Figure 6. Raman spectra of 3D nanoporous Si-based nanohybrids coated or interconnected with carbon, MWCNT and graphene nanosheets (GNS) prepared by microwave assisted solid state (MW-SS) and (MW-ST) methods.

respectively, via a magnesiothermic reduction process. Raman spectra (Figure 6a) illustrate that the sharp and intense peak of porous Si located at 514 cm^{-1} is associated with the Si–Si stretching mode and a small peak at 961 cm^{-1} is owing to the stretching mode of amorphous Si–Si, which are similar to the all three Si obtained from RH, BC, and SB, respectively. It is reported that commercial Si is located at 497 cm^{-1}. The Raman peak of porous Si is shifted 17 cm^{-1} toward a lower frequency.[35] Compared to commercial Si powders, porous Si prepared by MW-MR has a lesser amorphous Si phase on the surface rather than Si prepared by other conventional processes, as evidenced by relatively high frequency of silicon phonon vibration. This reveals that the obtained Si is porous and crystalline in nature, as manifested by above XRD results. Moreover, changes in profile and shape of the Raman peaks may have resulted mostly from the confinement of optical phonons from Si nanocrystals. When the diameters of Si nanocrystals are small, the Raman peak width increases and becomes more asymmetric.[35] To further improve the electronic conductivity of the porous Si, we decorated carbon, MWCNT, and GNS coating on Si extracted from RH as an example. Raman spectra of carbon/Si, MWCNT/Si and GNS/Si are illustrated in Figure 6b (inset). In all the three types of nanohybrids, the characteristic bands of both Si as well as dimensionally modulated carbon-based materials (carbon, MWCNT, and GNS) are shown in Figure 6b (inset). The sharp peak at 519 cm^{-1} and small hump at 955 cm^{-1} are related to the crystalline and amorphous forms of Si–Si stretching mode, respectively. On the other hand, the two other peaks at 1364 and 1606 cm^{-1} in the case of the Si/C hybrid, 1358 and 1574 cm^{-1} for the Si/MWCNT, and 1352 and 1606 cm^{-1} for the Si/GNS are assigned to the D-band (disorder band) and G-band (graphite band) of carbon, respectively.[27] This peak confirms the carbon, MWCNT, and GNS decorated on Si. The G-mode is the symmetry-allowed tangential E_{2g} mode, where as the D and D′ modes are owing to the first-order double resonance Raman scattering process and reflect the presence of structural disorders on the graphite plane of the carbon-based materials. The peak intensity ratio I_D/I_G can be used to asses a useful index for evaluating the degree of crystallinity of various

DOI: 10.1021/sc500735a
ACS Sustainable Chem. Eng. 2015, 3, 224–236

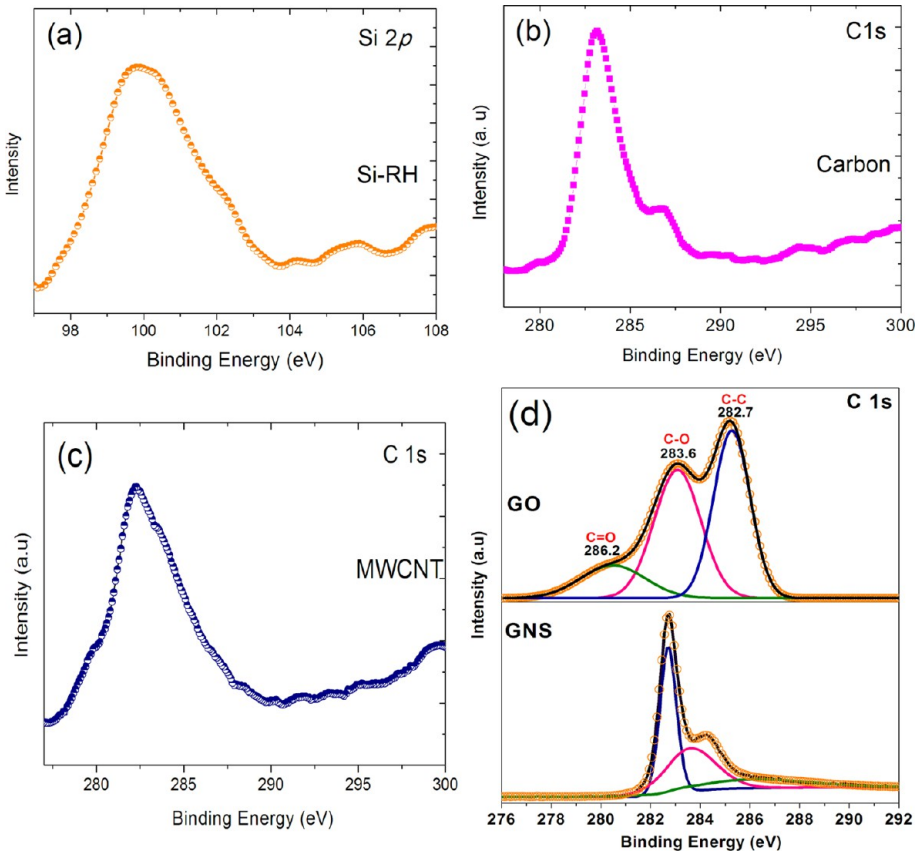

Figure 7. XPS spectra of Si-based nanohybrids prepared by microwave assisted solid state (MW-SS) and (MW-ST) methods (a) Si 2p spectrum of Si in the Si/C and C 1s spectra of (b) carbon in the Si/C (c) MWCNT in the Si/MWCNT (d) GNS in the Si/GNS and as-synthesized pristine GO.

carbon-based materials, i.e., higher the degree of ordering in the carbon material, smaller the ratio of I_D/I_G.[29] Here the value of I_D/I_G is 0.699 for carbon in Si/C, 0.839 for MWCNT in Si/MWCNT and 0.788 for GNS in Si/GNS. Hence, the Raman results obtained are owing to the fact that the carbon is orderly arranged, which is advantageous to attain effective electronic conduction between neighboring Si nanoparticles. It has been reported that this technique can be utilized to differentiate either a single layer or less than five layers by the position, shape and breadth of the 2D peak.[29] Figure 6b (inset) demonstrates 2D band (514 nm excitation) as a function of graphite layers, illustrating that the Si nanocrystals are decorated with the few layers of GNS. Thus, the data of Raman spectra corroborated with the XRD, XPS, and FE-SEM that the rapid MW-ST method employed here is an efficient process to produce Si/GNS, Si/MWCNT nanohybrids.

XPS Characterization. XPS can measure the surface compositions of the synthesized nanomaterials by determining the binding energy (BE) of photoelectrons ejected when X-rays are irradiated on the surface of Si and their carbon-based nanohybrid materials. XPS is the surface sensitive analysis derived from the small (<10 nm) inelastic mean free path of the ejected photoelectrons. This permits the elemental composition (except for hydrogen) of the near surface region to be quantified. Figure 7a shows XPS spectra of Si 2p for the Si extracted via MW-MR reduction process. The broad peak between 99.8 and 100.3 eV is corresponding to the Si $2p_{1/2}$ and Si $2p_{3/2}$ orbitals from zero-valent Si, respectively. A very small hump was observed at about 105.4 eV, corresponding to the Si $2p_{1/2}$ and Si $2p_{3/2}$ orbitals from SiO_x, which is probably due to the increase in the surface area that leads to more reaction with oxygen from the atmosphere. Carbon peak C 1s spectra derived from Si/C and Si/MWCNT nanohybrids are shown in Figure 7b and c. The strong peak near 283.3 eV clearly designates the presence of carbon bonding and weaker peak near 287 eV designates the existence of residual graphitic carbon. Figure 7d shows the C 1s XPS spectra recorded before and after reduction of GO with Si nanocrystals subjecting to the MW-ST process. Figure 7d illustrates the C 1s spectrum of GO (after deconvolution), which clearly exhibits the lower BE feature at 284.4 eV corresponding to C—C carbon and the higher BE feature at 286.6 eV followed by a shoulder at 289 eV, which is usually assigned to C—OH and C═O from epoxide, hydroxyl, and carboxyl functionalities. After reduction of GO under the MW-ST process, the XPS spectrum of Si/GNS (Figure 7d) implies that the intensity of the bands corresponding to carboxyl, epoxide, and hydroxyl functionalities are significantly decreased. On the other hand, the sp^2 carbon network is maintained in GNS as designated by the C—C peak at 284 eV and the remarkable $\pi-\pi^*$ satellite peak at 288.2 eV is a characteristic peak of either conjugated or aromatic compound.

Electrochemical Performance. Figure 8a,c,e shows the lithiation−delithiation profiles of the Si (obtained from RH) denoted as Si_{RH}-based nanohybrids (Si/C, Si/GNS, and Si/MWCNT) electrodes at a rate of C/50, C/20 cycled from 0.01 to 1.0 V versus Li/Li^+. During the first lithiation (discharging) curve, two major plateaus appear at ∼0.3 and ∼0.1 V. In the following cycles, the absence of the former plateau is clearly denoted due to electrolyte decomposition coupled with the occurrence of solid electrolyte interface (SEI) on the electrode

DOI: 10.1021/sc500735a
ACS Sustainable Chem. Eng. 2015, 3, 224−236

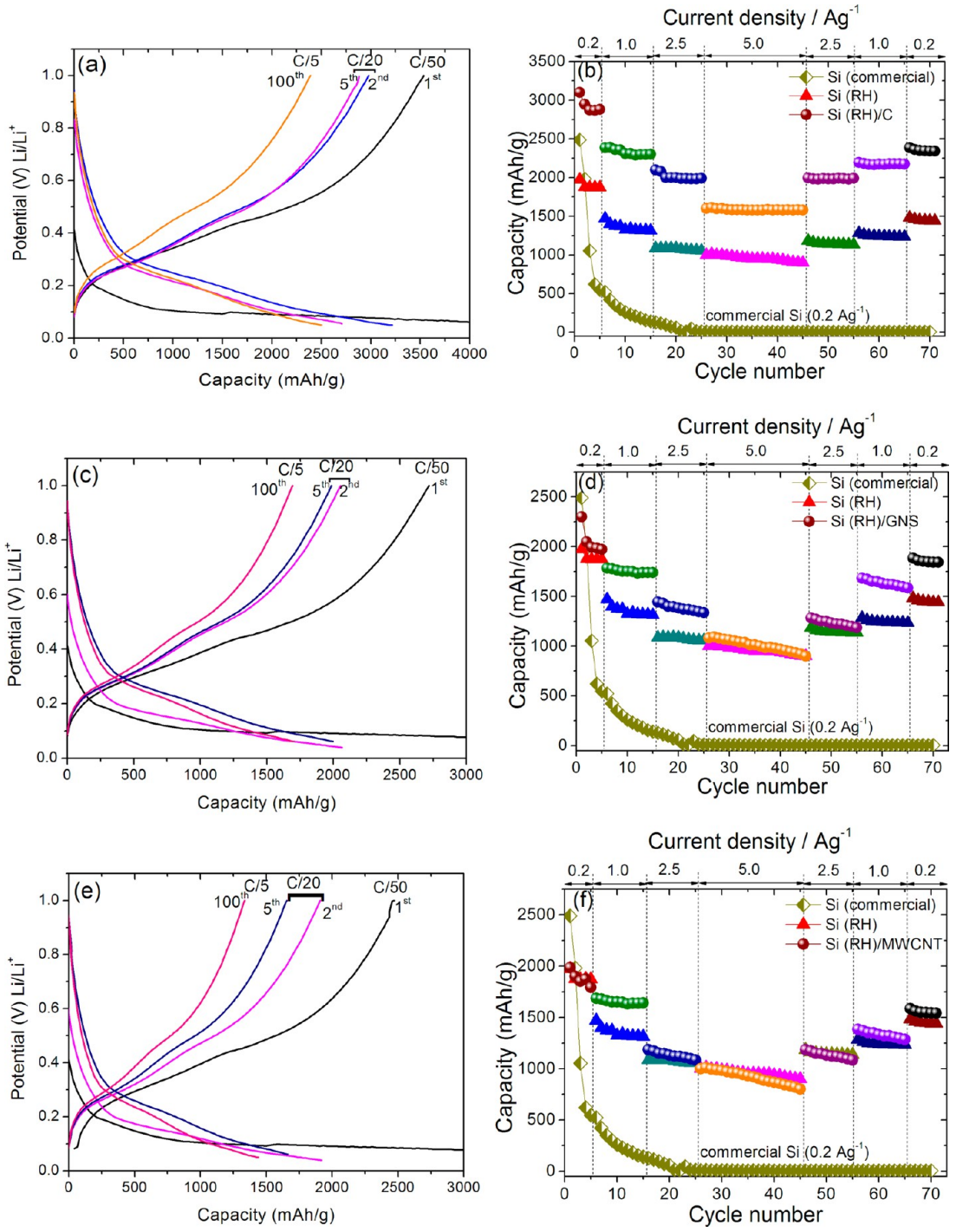

Figure 8. Comparative electrochemical lithiation−delithiation profiles of the samples (a) Si/C, (c) Si/GNS, and (e) Si/MWCNT in different C-rates from 0.01 to 1.0 V versus Li/Li^+ and power capability plots of the samples (b) Si/C,(d) Si/GNS, (f) Si/MWCNT versus cycle number, respectively, and different current densities A g^{-1}. Note that the capacity and current density are based on the whole composite mass (mAh g^{-1} composite). For comparative purposes, commercial Si is provided. The current density for commercial Si was kept constant at 0.2 A g^{-1}.

surface.[36] Moreover, the alloying reaction between crystalline Si and Li indicated the occurrence of a long flat plateau at ∼0.1 V.[21] The carbon-decorated Si anode (Figure 8a) shows an initial delithiation capacity of 3518 mAh g^{-1} at a rate of C/50, with a Coulombic efficiency of 77.5%. The Si/C anode further stabilizes delithiation capacity of 2958 mAh g^{-1} at a rate of C/20 in the 2nd cycle, with a Coulombic efficiency of 92.9%. The capacity drops to 2381 mAh g^{-1} at a rate of C/5 after 100 cycles, with a Coulombic efficiency of 95.8%. These delithiation capacities of Si/C values are higher than (5 to 7 times) the theoretical capacity of graphite (372 mAh g^{-1}). On the other hand, the MW-ST synthesized Si_{RH}/GNS anode (Figure 8c) exhibits a delithiation capacity of 2714 mAh g^{-1} in the 2nd cycle and 1681 mAh g^{-1} at a rate of C/5 in the 100th cycle, with a Coulombic efficiency of 99.3%. Figure 8e exhibits the Si_{RH}/MWCNT nanohybrid anode, which offers a delithiation capacity of 1903 mAh g^{-1} in the 2nd cycle and 1321 mAh g^{-1} in at a rate of C/5 in the 100th cycle, with a Coulombic

DOI: 10.1021/sc500735a
ACS Sustainable Chem. Eng. 2015, 3, 224−236

efficiency of 99.6%. It is suggested that the Coulombic efficiency after the 1st cycle is enhanced in all the Si-based nanohybrids samples possessing the buffer nanoporous is more desirable to suppress the structure destruction of the carbon framework and facilitate better lithium extraction.[37−39] However, the among three types of Si-based nanohybrids, carbon decorated Si obtained via MW-SS offers highest delithiation capacity of 2958 mAh g^{-1} in the 2nd cycle at a rate of C/20. Moreover, Si/GNS exhibits better cycling performance rather than Si/MWCNT, as shown in Figure 8c,e, respectively.

Figure 8b,d,f compares the rate capability of nanostructured Si_{RH}/C, Si_{RH}/GNS, and Si_{RH}/MWCNT. Here, the current density increases gradually from 0.2 Ag^{-1} to 5.0 Ag^{-1} and finally returns to 0.2 Ag^{-1}. While a constant current density of 0.2 Ag^{-1} has been applied for commercial-Si throughout the cycles, the delithiation capacity of commercial Si is rapidly decreased and almost lost at as early as 20 cycles due to lithiation of Si into crystalline $Li_{15}Si_4$. In contrast, nanoporous Si_{RH}/C, Si_{RH}/MWCNT, and Si_{RH}/GNS show much better cyclabilities than commercial Si. This is because Si-based nanohybrids are likely to be lithiated into amorphous Li_xSi alloy, as illustrated in Figure 8b,d,f. Besides, the rate capability is plotted against the cycle number in Figure 8b,d,f in which nano Si_{RH}/C, Si_{RH}/GNS, and Si_{RH}/MWCNT always show better rate capabilities at current densities of 0.2, 1.0, 2.5, and 5.0 A g^{-1}. Particularly, Si_{RH}/C offers 2387 mAh g^{-1} at a current density of 0.1 A g^{-1}. When the current density of 0.1 A g^{-1} resumed, the reversible capacity back to 2175 mAh g^{-1} of Si_{RH}/C. We compared the cycling performance of our pristine nanoporous Si and Si-based nanohybrids with the commercial Si nanopowder electrode without any nanoporous structure and with particle sizes ranging from 100−200 nm (Figure 4g) under the same electrochemical reaction conditions. We observed that electrochemical performance of the 3D nanoporous silicon and its respective nanohybrids with carbon, GNS, and MWCNT is much enhanced than that of the commercial Si.

Figure 9a shows the curves of discharge capacity versus cycle number for the commercial silicon nanoparticles, 3D nanoporous silicon, and Si_{RH}-based nanohybrids such as Si_{RH}/C, Si_{RH}/GNS, and Si_{RH}/MWCNT at a galvanostatic discharge rate of C/5 from 0.01 to 1.0 V versus Li/Li^+. It was found that the electrode fabricated from the commercial Si nanoparticles offered a high discharge capacity only for the initial few cycles. Subsequently, the capacity fading occurred rapidly owing to large volume change (>300%) during the formation of Li_xSi (Li-alloying) and restoration of Si (dealloying) processes, which leads to electrical disconnection between particles and cracking of electrode film coated in the current collector, as clearly shown in the FE-SEM images before and after 100 cycling in Figure 9b,c.[40,41] In contrast, the Si that was obtained from the MW-MR method demonstrates a considerably enhanced cyclability due to a unique nanoporous structure that provides sufficient void-space to accommodate the large volume change. Besides, the cycling performance of Si-based nanohybrids is further improved. After 200 cycles, Si-based nanohybrids such as Si_{RH}/C, Si_{RH}/GNS, and Si_{RH}/MWCNT offered enhanced capacities of 1997, 1290, and 1166 mAh g^{-1} respectively, which were higher than that of pristine Si extracted from RH, maintaining a reversible capacity of ∼956 mAh g^{-1}.

The improved electrochemical performance of pristine 3D nanoporous Si_{RH}, Si_{RH}/C, Si_{RH}/GNS, and Si_{RH} /MWCNT nanohybrids is attributed to its highly crystalline internal

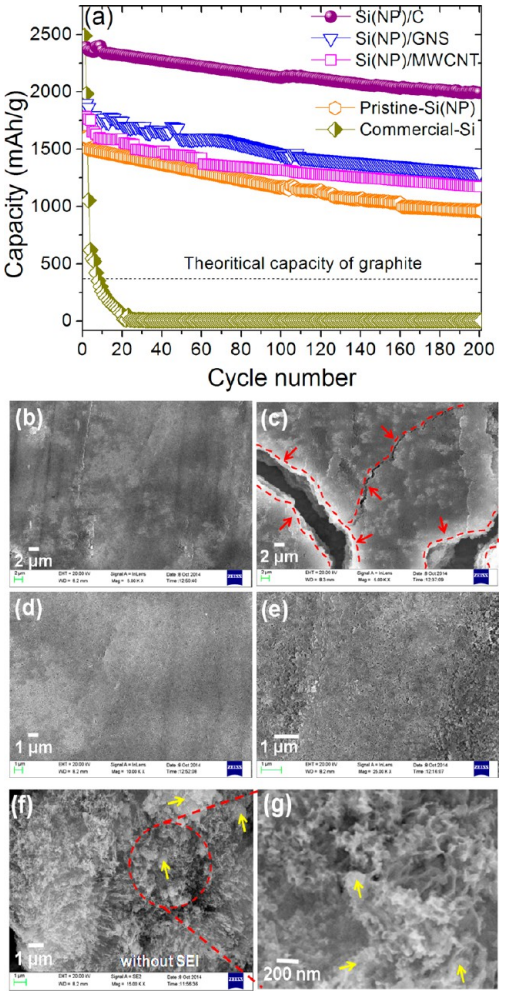

Figure 9. (a) Comparative galvanostatic cycling of pristine nanoporous Si_{RH} extracted from agricultural residue (RH) and their respective nanohybrids such as Si/C, Si/GNS, and Si/MWCNT at C/5 rate cycled from 0.01 to 1.0 V versus Li/Li^+. Note that the capacity is based on the whole composite mass (mAh g^{-1} composite). Comparison of commercial Si is also provided at C/5 rate. Comparison of FE-SEM images of commercial Si (b) before and (c) after the 100 cycles and comparison of FE-SEM images of 3D nanoporous Si_{RH} obtained by MW-MR (d) before and (e) after the galvanostatic cycles. FE-SEM image (f) of the electrode that was washed first with acetonitrile and then with diluted HCl acid to remove the solid-electrolyte interphase (SEI) and magnified image (f) to show the porous nature of Si, yellow arrows in the image indicate super-P conducting carbon additives.

nanoporous structure and its ability to act as a "buffer nanospace" and further accommodate the large volume change during the lithiation/delithiation process. Hence, it also suggests the lower internal resistance due to the presence of carbon-based materials and they provide space to accommodate expansion and contraction of the nanoporous Si_{RH} without cracking the anode as clearly shown in FE-SEM image before and after 100 cycles in Figure 9d,e.[38,39] Moreover, to study the electrode morphology after 100 cycles, the coin cell electrode was disassembled and washed first with acetonitrile and with hydrochloric acid to remove the solid electrolyte interphase (SEI) to examine whether nanoporous structure existed within the Si_{RH} using FE-SEM. It was observed that the Si_{RH} prepared from MW-SS still showed high porosity into the nanoporous framework, as displayed in Figure 9f and the magnified image

DOI: 10.1021/sc500735a
ACS Sustainable Chem. Eng. 2015, 3, 224−236

shown in Figure 9g. To verify this, fully delithiated (i) commercial Si nanoparticles, (ii) 3D nanoporous Si_{RH}, (iii) before and after carbon/GNS/MWCNT interconnected nanoporous Si_{RH}-based electrodes were evaluated using electrochemical impedance spectroscopy (EIS) after 100 cycles.

EIS measurements were demonstrated to substantiate the electrochemical performance of the pristine 3D nanoporous Si_{RH} obtained from the MW assisted method, compared to the nanohybrids such as Si/C, Si/GNS, Si/MWCNT, and commercial Si. Figure 10 shows impedance spectra of the

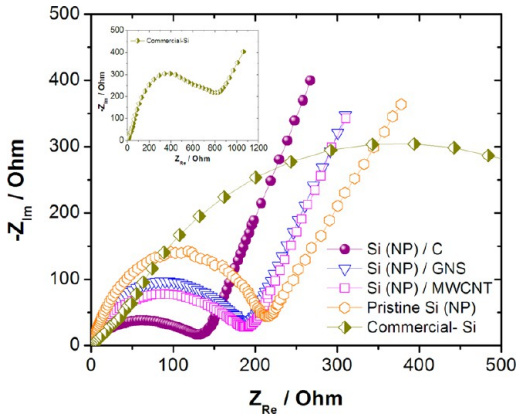

Figure 10. Impedance (EIS) measurement (Nyquist) plot of a commercial Si, 3D nanoporous Si_{RH}-synthesized via MW-SS process and their respective nanohybrids such as Si/C, Si/GNS, and Si/MWCNT after 100 cycles. All the measurements were performed in the delithiated state.

pristine 3D nanoporous Si_{RH}, Si/C, Si/GNS, and Si/MWCNT electrodes after 100 cycles and the commercial Si after 20 cycles. The high-to-medium frequency range semicircle corresponds to charge-transfer impedance on electrode–electrolyte interface.[34] Warburg impedance tail (straight line in the low frequency range) is attributed to impedance caused by bulk diffusion of ions into the active material of the electrode.[42,43] We observed that the large change occurred in the diameter of the semicircle of Si/C electrode is lesser than pristine nanoporous Si_{RH}, Si/GNS, Si/MWCNT and much lesser than commercial Si, respectively. This demonstrates that during the interfacial electrochemical reaction, the Si_{RH}, Si/C, Si/GNS, and Si/MWCNT electrodes exhibit lowest internal resistance. This can be ascribed by the stable nanoporous structure of Si and to a better availability of electrons and perhaps also Li-ions of the Si/C, Si/GNS, and Si/MWCNT nanohybrids upon cycling. It is also illustrated that the poor electrochemical performance of commercial Si anode is due to the electrical separation of the electrode during the cycling process (FE-SEM images, as shown in Figure 9c) arising due to the destruction of Si active materials layer coated on current collector (copper foil) and semiconducting nature.[44−46] Compared to aggregated commercial Si, the enhancement in electrochemical performance of the pristine porous Si_{RH}, Si/C, Si/GNS, and Si/MWCNT nanohybrids as a promising anode material for lithium ion batteries is attributed to the "synergistic effects" that arise due to the combination of nanoporous Si and dimensionally modulated carbons, coupled with subsequent increase in interparticle electrical conductivity and also in the rate of electron transport. Moreover, the cushion nature of 3D nanoporous Si_{RH}, 2D graphene, 1D MWCNT nanonetworks, and the carbon nanolayers works collectively to accommodate the severe volume expansion and there by suppress the aggregation and destruction of Si nanoparticles upon lithiation−delithiation processes, thus improving the structural stability.

CONCLUSIONS

In conclusion, we have successfully demonstrated the feasibility of synthesizing nanoporous Si particles by facile, rapid, energy-efficient microwave assisted solid-state (MW-SS) ashing followed by microwave assisted metallothermic reduction (MW-MR) techniques. We have developed an eco-friendly and low-cost sustainable method to extract high value 3D nanoporous Si directly from naturally occurring agricultural residues such as SB, BC, and RH, where Si naturally exists in the form of SiO_2. Significantly, this method does not require any reduced gas atmosphere or postannealing at higher temperatures to synthesize 3D nanoporous Si and its nanohybrids within a few minutes. Therefore, both the MW-SS and MW-MR processes are easy to scale up. The highly porous interconnected 3D network of Si was subsequently decorated with dimensionally modulated carbon-based anode materials that offer excellent delithiation capacities and rate capabilities through better accommodation of the structural changes than bulk commercial Si. This low-cost and sustainable method brings a new outlook in the rapid synthesis of 3D nanoporous Si from the most popular crops that can be sustainable natural and earth-abundant bioresources to meet the escalating requirements for nanostructured silicon in clean energy conversion as well as in storage applications.

ASSOCIATED CONTENT

Supporting Information

Digital photographic image of GO nanostructured foam, thermogravimetric (TGA) analysis of SB, BC, and RH raw materials heated from room temperature to 1000 °C in oxygen atmosphere, thermogravimetric (TGA-DTA) results of Mg powder and RH ash (SiO_2) heated from room temperature to 1000 °C in N_2 atmosphere, FE-SEM micrographs, comparison of conventional and microwave assisted (MW-MR) methods, chemical composition of RH, BC, and SB after burning out into ash, and comparative table for SiO_2 to Si conversion yield. This material is available free of charge via the Internet at http://pubs.acs.org.

AUTHOR INFORMATION

Corresponding Author

*A. Vadivel Murugan. E-mail: avmrajeshwar@gmail.com; avmurugan.nst@pondiuni.edu.in. Tel: +91-413-2654975.

Notes

The authors declare no competing financial interest.

ACKNOWLEDGMENTS

The Authors express their gratitude toward the following funding agencies: Department of Science & Technology (DST), Government of India, New Delhi, Science and Engineering Research Board (SERB) under project No. SR/S1/PC-31/2011. Ms. S. Praneetha specially thanks DST-SERB for providing research fellowship. We also thank Central instrumentation facilities (CIF), Pondicherry University for materials characterization.

DOI: 10.1021/sc500735a
ACS Sustainable Chem. Eng. 2015, 3, 224−236

REFERENCES

(1) Manthiram, A.; Vadivel Murugan, A.; Sarkar, A.; Muraliganth, T. Nanostructured electrode materials for electrochemical energy storage and conversion. *Energy Environ. Sci.* **2008**, *1*, 621−638.

(2) Manthiram, A. Materials challenges and opportunities of lithium ion batteries. *J. Phys. Chem. Lett.* **2011**, *2*, 176−184.

(3) Jung, D. S.; Ryou, M.-H.; Sung, Y. J.; Park, S. B.; Choi, J. W. Recycling rice husks for high-capacity lithium battery anodes. *PNAS* **2013**, *110*, 12229−12234.

(4) Favors, Z.; Wang, W.; Bay, H. H.; Mutlu, Z.; Ahmed, K.; Liu, C.; Ozkan, M.; Ozkan, C. S. Scalable synthesis of nano-silicon from beach sand for long cycle life Li-ion batteries. *Sci. Rep.* **2014**, *4*, 5623.

(5) Liu, N.; Huo, K.; McDowell, M. T.; Zhao, J.; Cui, Y. Rice husks as a sustainable source of nanostructured silicon for high performance Li-ion battery anodes. *Sci. Rep.* **2013**, *3*, 1919.

(6) Atkins, T. M.; Thibert, A.; Larsen, D. S.; Dey, S.; Browning, N. D.; Kauzlarich, S. M. Femtosecond ligand/core dynamics of microwave-assisted synthesized silicon quantum dots in aqueous solution. *J. Am. Chem. Soc.* **2011**, *133*, 20664−20667.

(7) Bang, B. M.; Lee, J. I.; Kim, H.; Cho, J.; Park, S. High-performance macroporous bulk silicon anodes synthesized by template-free chemical etching. *Adv. Energy Mater.* **2012**, *2*, 878−883.

(8) Jia, H.; Gao, P.; Yang, J.; Wang, J.; Nuli, Y.; Yang, Z. Novel three-dimensional mesoporous silicon for high power lithium-ion battery anode material. *Adv. Energy Mater.* **2011**, *1*, 1036−1039.

(9) Meng, T. Inorganic photovoltaic solar cells: Silicon and beyond. *Electrochem. Soc. Interface* **2008**, *17*, 30−35.

(10) Sarti, D.; Einhaus, R. Silicon feedstock for the multi-crystalline photovoltaic industry. *Sol. Energy Mater. Sol. Cells* **2002**, *72*, 27−40.

(11) Salanti, A.; Zoia, L.; Orlandi, M.; Zanini, F.; Elegir, G. Structural characterization and antioxidant activity evaluation of lignins from rice husk. *J. Agric. Food Chem.* **2010**, *58*, 10049−10055.

(12) Chen, H.; Wang, W.; Martin, J. C.; Oliphant, A. J.; Doerr, P. A.; Xu, J. F.; DeBorn, M. K.; Chen, C.; Sun, L. Extraction of lignocellulose and synthesis of porous silica nanoparticle frm rice husks: A comprehensive utilization of rice husk biomass. *ACS Sustainable Chem. Eng.* **2013**, *1*, 254−259.

(13) Struyf, E.; Smis, A.; Van Damme, S.; Meire, P.; Conley, D. J. The global biogeo-chemical silicon cycle. *Silicon.* **2010**, *1*, 207−213.

(14) Ma, J. F.; Yamaji, N. Silicon uptake and accumulation in higher plants. *Trends Plant Sci.* **2006**, *11*, 392−397.

(15) Epstein, E. Silicon: Its manifold roles in plants. *Ann. Appl. Biol.* **2009**, *155*, 155−160.

(16) Epstein, E. The Anomaly of silicon in plant biology. *Proc. Natl. Acad. Sci. U. S. A.* **1994**, *91*, 11−17.

(17) Wu, H.; Chan, G.; Choi, J. W.; Ryu, I.; Yao, Y.; McDowell, M. T.; Lee, S. W.; Jackson, A.; Yang, Y.; Hu, L. B.; Cui, Y. Stable cycling of double-walled silicon nanotube battery anodes through solid-electrolyte interphase control. *Nat. Nanotechnol.* **2012**, *7*, 310−315.

(18) Ge, M. Y.; Rong, J. P.; Fang, X.; Zhou, C. W. Porous doped silicon nanowires for lithium ion battery anode with long cycle life. *Nano Lett.* **2012**, *12*, 2318−2323.

(19) Bang, B. M.; Kim, H.; Song, H. K.; Cho, J.; Park, S. Scalable approach to multi-dimensional bulk Si anodes *via* metal-assisted chemical etching. *Energy Environ. Sci.* **2011**, *4*, 5013−5019.

(20) Magasinski, A.; Dixon, P.; Hertzberg, B.; Kvit, A.; Ayala, J.; Yushin, G. High-performance lithium-ion anodes using a hierarchical bottom-up approach. *Nat. Mater.* **2010**, *9*, 353−358.

(21) Cui, L. F.; Yang, Y.; Hsu, C. M.; Cui, Y. Carbon−silicon core−shell nanowires as high capacity electrode for lithium ion batteries. *Nano Lett.* **2009**, *9*, 3370−3374.

(22) Park, M. H.; Kim, M. G.; Joo, J.; Kim, K.; Kim, J.; Ahn, S.; Cui, Y.; Cho, J. Silicon nanotube battery anodes. *Nano Lett.* **2009**, *9*, 3844−3847.

(23) Kim, H.; Han, B.; Choo, J.; Cho, J. Three-dimensional porous silicon particles for use in high-performance lithium secondary batteries. *Angew. Chem., Int. Ed.* **2008**, *47*, 10151−10154.

(24) Cho, J. Porous Si anode materials for lithium rechargeable batteries. *J. Mater. Chem.* **2010**, *20*, 4009−4014.

(25) Vadivel Murugan, A.; Muraliganth, T.; Ferreira, P. J.; Manthiram, A. Dimensionally modulated, single-crystalline $LiMPO_4$ (M = Mn, Fe, Co, and Ni) with nano-thumb like shapes for high-power energy storage. *Inorg. Chem.* **2009**, *48*, 946−952.

(26) O'Mara, C. O.; Herring, B.; Hont, P. *Handbook of semiconductor silicon technology*; Elsevier Science: Amsterdam, 1990.

(27) Vadivel Murugan, A.; Muraliganth, T.; Manthiram, A. Comparison of microwave assisted solvothermal and hydrothermal syntheses of $LiFePO_4$/C nanocomposite cathodes for lithium ion batteries. *J. Phys. Chem. C* **2008**, *112*, 14665−15671.

(28) Vadivel Murugan, A.; Muraliganth, T.; Manthiram, A. Rapid, facile microwave- solvothermal synthesis of graphene nanosheets and their polyaniline nano-composites for energy storage. *Chem. Mater.* **2009**, *21*, 5004−5006.

(29) Praneetha, S.; Vadivel Murugan, A. A rapid, one-pot microwave-solvothermal synthesis of a hierarchical nanostructured graphene/$LiFePO_4$ hybrid as a high performance cathode for lithium ion batteries. *RSC Adv.* **2013**, *3*, 25403−25409.

(30) Barrett, E. P.; Joyner, L. G.; Halenda, P. P. The determination of pore volume and area distributions in porous substances. I. Computations from nitrogen isotherms. *J. Am. Chem. Soc.* **1951**, *73*, 373−380.

(31) Xing, A.; Tian, S.; Tang, H.; Losic, D.; Bao, Z. Mesoporous silicon engineered by the reduction of biosilica from rice husk as a high-performance anode for lithium-ion batteries. *RSC Adv.* **2013**, *3*, 10145−10149.

(32) Sharma, N. K.; Williams, W. S.; Zangvil, A. Formation and structure of silicon carbide whiskers from rice hulls. *J. Am. Ceram. Soc.* **1984**, *67*, 715−720.

(33) Gaberscek, M.; Jamnik, J. Impact of electrochemical wiring topology on the kinetics of insertion electrodes. *Solid State Ionics* **2006**, *177*, 2647−2651.

(34) Guo, Y. G.; Hu, Y. S.; Sigle, W.; Maier, J. Superior electrode performance of nanostructured mesoporous TiO_2(Anatase) through efficient hierarchical mixed conducting networks. *Adv. Mater.* **2007**, *19*, 2087−2091.

(35) Lam, C.; Zhang, Y. F.; Tang, Y. H.; Lee, C. S.; Bello, I.; Lee, S. T. Large-scale synthesis of ultrafine Si nanoparticles by ball milling. *J.Cryst. Growth* **2000**, *220*, 466−470.

(36) Kim, T.; Mo, Y. H.; Nahm, K. S.; Oh, S. M. J. Carbon nanotubes(CNTs) as a buffer layer in silicon/CNTs composite electrodes for lithium secondary batteries. *J. Power Sources.* **2006**, *162*, 1275−1281.

(37) Cakan, R. D.; Titirici, M.-M.; Antonietti, M.; Cui, G.; Maier, J.; Hu, Y.-S. Hydrothermal carbon spheres containing silicon nanoparticles: synthesis and lithium storage performance. *Chem. Commun.* **2008**, *32*, 3759−3761.

(38) Luo, J.; Zhao, X.; Wu, J.; Jang, H. D.; Kung, H. H.; Huang, J. Crumpled graphene- encapsulated Si nanoparticles for lithium ion battery anodes. *J. Phys. Chem. Lett.* **2012**, *3*, 1824−1829.

(39) Zhou, G.; Li, F.; Cheng, H.-M. Progress in flexible lithium batteries and future prospects. *Energy Environ. Sci.* **2014**, *7*, 1307−1338.

(40) Saint, J.; Morcrette; Larcher, D.; Laffont, L.; Beattie, S.; Peres, J. P.; Talaga, D.; Couzi, M.; Tarascon, J. M. Towards a fundamental understanding of the improved electrochemical performance of silicon-carbon composites. *Adv. Funct. Mater.* **2007**, *17*, 1765−1774.

(41) Yu, Y.; Gu, L.; Zhu, C.; Tsukimoto, S.; van Aken, A. P.; Maier, J. Reversible storage of lithium in silver-coated three-dimensional macroporous silicon. *Adv. Mater.* **2010**, *22*, 2247−2250.

(42) Gao, P.; Fu, J.; Yang, J.; Lv, R.; Wang, J.; Nuli, Y.; Tang, X. Microporous carbon coated silicon core/shell nanocomposite *via in situ* polymerization for advanced Li-ion battery anode material. *Phys. Chem. Chem. Phys.* **2009**, *11*, 11101−11105.

(43) Wang, X.; Xiang, Q.; Liu, B.; Wang, L.; Luo, T.; Chen, D.; Shen, G. TiO_2 modified FeS Nanostructures with enhanced electrochemical performance for lithium-ion batteries. *Sci. Rep* **2013**, *3*, 1−8.

(44) Oumellal, Y.; Delpuech, N.; Mazouzi, D.; Dupre, N.; Gaubicher, J.; Moreau, P.; Soudan, P.; Lestriez, B.; Guyomard, D. J. J. The failure

DOI: 10.1021/sc500735a
ACS Sustainable Chem. Eng. 2015, 3, 224−236

mechanism of nano-sized Si-based negative electrodes for lithium ion batteries. *J. Mater. Chem.* **2011**, *21*, 6201−6208.
(45) Evanoff, K.; Magasinski, A.; Yang, J.; Yushin, G. Nanosilicon-coated graphene granules as anodes for Li-ion batteries. *Adv. Energy Mater.* **2011**, *1*, 495−498.
(46) Nguyen, H. T.; Yao, F.; Zamfir, M. R.; Biswas, C.; So, K. P.; Lee, Y. H.; Kim, S. M.; Cha, S. N.; Kim, J. M.; Pribat, D. Highly interconnected Si nanowires for improved stability Li-ion battery anodes. *Adv. Energy Mater.* **2011**, *1*, 1154−1161.

DOI: 10.1021/sc500735a
ACS Sustainable Chem. Eng. 2015, 3, 224−236